Composites Part B 236 (2022) 109822

Contents lists available at ScienceDirect

Composites Part B

journal homepage: www.elsevier.com/locate/compositesb

Heterostructures of mixed metal oxides ($ZnMnO_3$/ZnO) synthesized by a wet-chemical approach and their application for the electrochemical detection of the drug chlorpromazine

Karuppaiah Balamurugan [a,1], Raj Karthik [b,1], Shen-Ming Chen [a,*], Ramaraj Sukanya [c], Bhuvaneswari Thasma Subramanian [d], Valsala Madhavan Nair Biju [d], Jae-Jin Shim [b,*], Carmel B. Breslin [c]

[a] Electroanalysis and Bioelectrochemistry Lab, Department of Chemical Engineering and Biotechnology, National Taipei University of Technology, No. 1, Section 3, Chung-Hsiao East Road, Taipei, 106, Taiwan
[b] School of Chemical Engineering, Yeungnam University, Gyeongsan, Gyeongbuk, 38541, Republic of Korea
[c] Department of Chemistry, Maynooth University, Maynooth, Co. Kildare, W23F2H6, Ireland
[d] Department of Chemistry, National Institute of Technology, Trichy, 15, Tamil Nadu, India

ARTICLE INFO

Keywords:
Heterostructure
$ZnMnO_3$/ZnO NPs
Electrochemical sensor
Psychotic drug
Chlorpromazine sensor

ABSTRACT

Materials development using heterostructures is generally considered an efficient method for developing electrocatalysts. However, it still faces many challenges, such as instability and accurate phase mixing ratio of metals. On the other hand, the excessive consumption of drugs such as chlorpromazine (CPMZ) leads to several serious human diseases. Therefore, the accurate detection and determination of CPMZ is essential. In this view, a highly efficient electrochemical sensor based on a heterostructure of $ZnMnO_3$/ZnO NPs/GCE was fabricated to detect the psychotic drug CPMZ. The heterostructure of cubic $ZnMnO_3$ (ZMO) and hexagonal zinc oxide nanoparticles (ZMO/ZnO NPs) was synthesized by a simple co-precipitation method followed by thermal calcination. The as-prepared material crystallinity and average crystal size (26 nm) were analyzed by p-XRD. The morphology of the ZMO/ZnO NPs was analyzed by SEM and HR-TEM, which revealed the formation of non-uniform spherical and hexagonal nanoparticles with a size of ~10-30 nm. FT-IR and XPS were used to investigate the functional groups and oxidation states of the ZMO/ZnO NPs. The electrochemical properties of the ZMO/ZnO NPs/GCE were analyzed by EIS, CV, and DPV methods. ZMO/ZnO/GCE has improved electrochemical activity for detecting CPMZ. In addition, the ZMO/ZnO/GCE electrochemical probe has two linear ranges (0.05–125.55 μM and 185.55–1625 μM) and good sensitivity (0.760 μA μM^{-1} cm^{-2}) with a low detection limit of 0.019 μM. Analysis of real samples was performed in human blood serum and urine, and the recoveries of CPMZ were 96–100% and 98–100%, respectively.

1. Introduction

Chlorpromazine (CPMZ), which belongs to the phenothiazine group of drugs, is a traditional antipsychotic drug. It is used to treat psychotic disorders such as manic depression or schizophrenia in adults. CPMZ is also used for anxiety before surgery, nausea, vomiting, acute intermittent porphyria, chronic hiccups, and symptoms of tetanus. CPMZ strongly blocks the dopamine D2 receptor and causes extrapyramidal motor side effects like tremors, muscle contractions, abnormal pigmentation of the eyelids, musculoskeletal disorders, cataracts, and accommodation disorders. Therefore, the efficient detection and determination of chlorpromazine has become an important research topic [1,2]. Several analytical methods have been developed for the study of CPMZ, including spectrophotometry, gas chromatography (GC), high-performance liquid chromatography (HPLC), and electrochemiluminescence [3–7]. These methods provide good sensitivity and selectivity for CPMZ determination, but they are not user-friendly, more time-consuming, require sophisticated instrumentation and specialized

* Corresponding authors.
E-mail addresses: smchen78@ms15.hinet.net (S.-M. Chen), jjshim@yu.ac.kr (J.-J. Shim).
[1] Authors K. Balamurugan and R. Karthik contributed equally to this manuscript.

https://doi.org/10.1016/j.compositesb.2022.109822
Received 7 December 2021; Received in revised form 4 March 2022; Accepted 10 March 2022
Available online 23 March 2022

training, and are very expensive compared to electrochemical methods. Moreover, electrochemical methods are practical analytical tools for detecting target molecules due to their feasibility, cost-effectiveness, portability, and notable sensitivity with selectivity [8–11].

In recent years, binary transition metal oxides (BTMOs) have received much attention as they can exhibit various oxidation states with improved electrical conductivity, thermal and structural stability [12]. In particular, manganese-containing oxides are attractive as manganese is earth-abundant, has low toxicity, exists in various oxidation states, and can be combined with divalent metals to give attractive structural, physical, and chemical properties [13–16]. Likewise, zinc-based oxides are exciting materials, as ZnO has low toxicity, excellent chemical, thermal durability, and oxygen deficiency. Accordingly, it has been employed as a functional material for various applications such as UV-lasers, solar cells, photoluminescence, and gas sensors [17–22]. The significant difference between the electronegativity of zinc and oxygen provides a strong ionic nature, which improves the adsorption and recognition of target molecules. Indeed, it has been successfully used as electrode material in many electrochemical sensor applications [19,23–25].

When manganese is combined with zinc, the resulting zinc-manganese oxide displays new properties. It exhibits two phases with manganese in different oxidation states. For example, $ZnMn_2O_4$ is a tetragonal spinel structure and has been studied for various applications such as supercapacitors, lithium-ion batteries (LIB), thermistors, and electrochemical sensors [26–29]. In contrast, $ZnMnO_3$ (ZMO) is a cubic spinel phase of the ilmenite type in which manganese has the +4-oxidation state, and its magnetic properties have been studied by several researchers [30–33]. In LIB studies, it has been shown that ZMO has superior discharge capacity compared to the individual ZnO or MnO_2 oxides [34] and has very good long-term stability as an anode material [35].

Another approach in the design of metal oxide-based sensors is to form a heterostructure of two different metal oxides. These structures are attracting much attention because of the synergistic effects of the two various oxides. These heterostructures can lead to improved thermal and structural stability as well as electrical conductivity [36]. In particular, heterostructures and nanocomposites based on Fe_2O_3, Co_3O_4, NiO, CuO and ZnO, SnO_2, $NiCo_2S_4$ have been successfully used as electrochemical/biosensors. They provide better electrocatalytic activity and high sensitivity to target molecules than the single metal oxides electrocatalysts [37–46]. Indeed, a ZMO/ZnO heterostructure has been prepared from glycolate precursors and used as an anode material in LiB [47].

The solid-state synthesis of ZMO is well known [48], while ZMO has also been prepared from nitrate precursors using the sol-gel method [49]. Porous ZMO spherulites have also been synthesized by a carbonate precipitation method [34], and *Su* et al. [50] formed microspheres of ZMO by refluxing the Zn and Mn glycolate precursors. In addition, the hydrothermal method can be used, and this approach has been employed by *Geng* et al. [35] to form a coaxial VGCF (vapor grown carbon fiber)/ZMO nanocomposite.

From the above discussions, we believe that a heterostructure composite of cubic zinc-manganese oxide and hexagonal zinc oxide nanoparticles ($ZnMnO_3$/ZnO NPs) can effectively enhance the electrocatalytic activity towards CPMZ detection. However, there are no studies on the electrochemical sensing applications of cubic $ZnMnO_3$. To the best of our knowledge, this is the first study on the synthesis of $ZnMnO_3$/ZnO heterostructures by a co-precipitation method and their application as an electrochemical sensor for CPMZ. $ZnMnO_3$/ZnO/GCE shows improved electrochemical performance in CPMZ sensing with excellent sensitivity, repeatability, good selectivity, and real sample analysis in biological fluids shows acceptable recovery results.

2. Experimental section

2.1. Reagents and chemicals

Zinc nitrate hexahydrate ($Zn(NO_3)_2.6H_2O$, 98%), manganese chloride tetrahydrate ($MnCl_2.4H_2O$, 99%), sodium hydroxide (NaOH, 98%), chlorpromazine (98%), monosodium hydrogen phosphate monohydrate ($NaH_2PO_4.H_2O$, 99%), and disodium hydrogen phosphate dihydrate ($Na_2HPO_4.2H_2O$, 99%), were supplied by Sigma-Aldrich, Taiwan. Different pH values of 0.05 M phosphate buffer solution (PBS) were prepared by dissolving the corresponding amount of $Na_2HPO_4.2H_2O$ and $NaH_2PO_4.H_2O$ in deionized water (DI) and used as supporting electrolyte. The pH of the supporting electrolyte was adjusted using aqueous HCl and NaOH solutions.

2.2. Synthesis of ZMO/ZnO NPs

The co-precipitation method was employed to synthesize the ZMO/ZnO NPs. In the typical synthesis procedure, $MnCl_2.4H_2O$ (0.1 M) and $Zn(NO_3)_2.6H_2O$ (0.2 M) were dissolved individually in 40 mL DI water under magnetic stirring. After complete dissolution, the two ionic solutions were poured into a 200 mL beaker which contained 50 mL DI water. Then, 40 mL of 0.5 M NaOH was added dropwise to the metal ion solution. The resulting solution was stirred for 12 h at 70 °C. Then the brown-colored precipitate was centrifuged and washed with water and ethanol. The resultant residue was dehydrated at 50 °C for 12 h in a hot air oven. Finally, the resulting hydroxide precursor was subjected to calcination at 600 °C for 4 h in a muffle furnace. The overall synthesis procedure and electrochemical application of ZMO/ZnO NPs is shown pictorially in Scheme 1.

2.3. Characterization techniques

To analyze the purity of the crystalline phase, p-XRD was recorded using the PANalytical X-pert PRO.MPD ($\lambda = 0.154$ nm) over the 2-theta range between 20 and 70°. The exact oxidation states and composition of the elements present in the ZMO/ZnO NPs were analyzed using XPS, Thermo-scientific multi-lab 2000. To verify the presence of metal-metal bonds and metal-oxygen bonds in ZMO/ZnO NPs, FT-IR was executed (JASCO FT-IR 4600 LE). Morphological investigations were carried out by SEM (SEM, Hitachi S-4800) and TEM (JEM 2100 F) techniques.

All electrochemical experiments were performed using equipment from CHI (cyclic voltammetry (CV), CHI611A; differential pulse voltammetry (DPV) CHI 900). Electrochemical analysis was performed in a 10 ml electrolytic cell containing 0.05 M PBS and three conventional electrodes: GCE - working electrode; KCl-saturated Ag/AgCl electrode - reference electrode; platinum wire - counter electrode. To avoid the presence of atmospheric oxygen, the electrochemical studies were carried out using a PBS purged with nitrogen gas at room temperature.

2.4. Design of the working electrode and analysis procedure for real samples

For the electrochemical experiments, the working electrode (GCE) was fabricated from ZMO/ZnO NPs using the following procedure. To clean the surface of GCE, it was gently polished using alumina slurry (0.05 μM) and rinsed with DI water. Then, a uniformly dispersed ZMO/ZnO NPs solution was prepared by sonicating 3 mg of ZMO/ZnO NPs in DI water (1 mL) for 10 min. Following this, 6 μL (3 mg/1 mL) of the ZMO/ZnO NPs suspension was coated on the well-cleaned GCE surface by the drop casting method. Then, the GCE was dried in a hot air oven (50 °C) for 10 min. Finally, the ZMO/ZnO NPs/GCE was used as the working electrode in EIS, CV, and DPV experiments.

For the analysis of real samples, human urine and blood serum samples were collected from healthy individuals. In the typical procedure, the collected biofluids (5 mL) were diluted with 10-fold PBS (pH

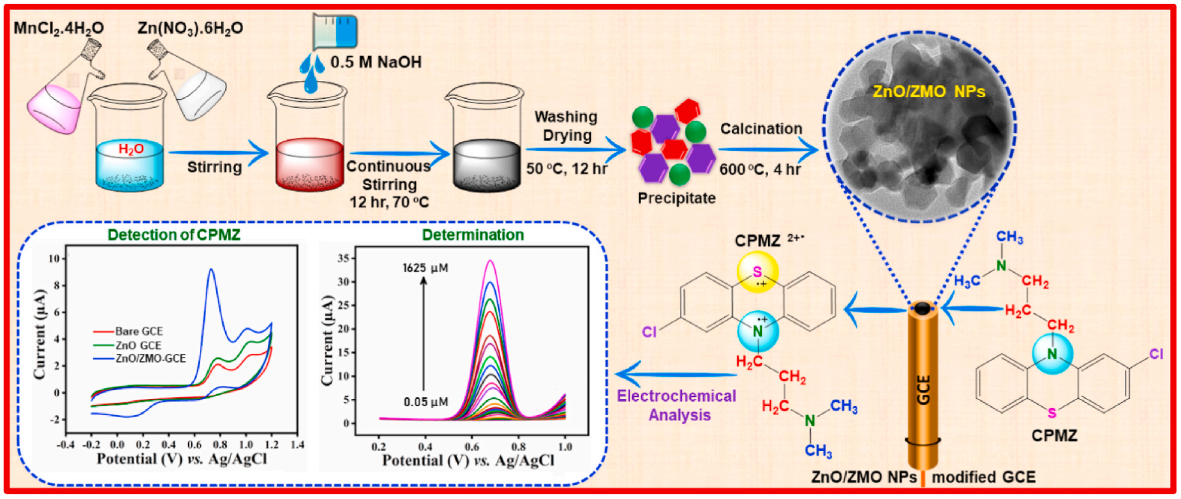

Scheme 1. Comprehensive synthesis method of ZMO/ZnO NPs and their electrocatalytic application for the detection of CPMZ.

7.0) and centrifuged at 6000 rpm. In practical applications, centrifuged blood serum, and urine samples (stock solutions) were spiked with a known concentration of CPMZ (ratio 1:1 CPMZ/stock solution) and subjected to DPV analysis by the standard addition method.

3. Results and discussion

3.1. FTIR and XRD studies

p-XRD was executed to verify the crystalline structure and phase formation of the ZMO/ZnO NPs, and the results are pictured in Fig. 1A. The XRD peaks at 2θ = 18.35°, 30.38°, 35.82°, 37.56°, 43.47°, 53.88°, 57.45°, and 63° were assigned to the following hkl planes: (111), (220), (311), (222), (400), (422), (511) and (440). This XRD pattern confirms the formation of cubic $ZnMnO_3$ with space group *F E* (JCPDS card: 00-019-1461) [47]. The remaining peaks at 2θ = 32°, 34.6°, 36.5°, 47.8°, 56.9°, 63°, 66.5°, 68.1°, and 69.2° were assigned to the hkl planes of (100), (002), (101), (102), (110), (103), (200), (112) and (201) of ZnO. This assignment agrees well with the JCPDS card: 01-079-0205 and confirms the formation of hexagonal ZnO with a space group of *P63mc*. For comparison, the XRD of ZnO is shown in Fig. S1A.

Moreover, no other peaks corresponding to manganese oxides such as MnO_2, Mn_2O_3, or Mn_3O_4 were found, proving the purity of the ZMO/ZnO NPs. In addition, the crystal size of the ZMO/ZnO NPs was calculated using the Debye-Scherer equation.

$$D(hkl) = K\lambda / \beta \cos \theta \quad (1)$$

In equation (1), D corresponds with the crystalline dimension, K is the shape factor, λ is the wavelength of X-rays, β represents the full width at half maximum of the peaks, and θ is the diffraction angle. Using equation (1), the average crystal size of ZMO/ZnO was calculated to be 26 nm.

The FTIR spectra of commercial ZnO and ZMO/ZnO NPs were analyzed between the wavelength of 4000–400 $cm^{-1,}$ and the corresponding data are displayed in Fig. S1B and Fig. 1B. In Figure *S1*B, the broad band evident at 3488 cm^{-1} is assigned to the O–H stretching vibration. The intense absorption band at 445 cm^{-1} refers to the Zn–O bond [51]. Meanwhile, the Zn–O vibrational band (458 cm^{-1}) was slightly shifted in the ZMO/ZnO NPs (Fig. 1B) due to the change of bond length by the presence of manganese [52]. Moreover, ZMO/ZnO NPs (Fig. 1B) show two more intense peaks at 525 cm^{-1} and 606 cm^{-1} due to the stretching of M-O-M and M – O bonds of manganese and zinc, respectively. The small band at 1008 cm^{-1} is related to the Mn–O–H vibrational band [53]. The remaining peaks between 800 and 1600 cm^{-1} are due to the nitrate salt of the metal ions and other precursors [52]. The p-XRD and FTIR analysis confirm the successful formation of ZMO/ZnO NPs heterostructure.

3.2. XPS analysis of ZMO/ZnO

The XPS spectrum provides information on the oxidation level and kinetic energy of the elements present in the materials. To know the surface composition and the exact valency of the elements present in the ZMO/ZnO NPs, XPS analysis was performed, and the results are exhibited in Fig. 2. From Fig. 2A, the overview spectrum of ZMO/ZnO NPs confirms the existence of zinc, manganese and oxygen. The core-

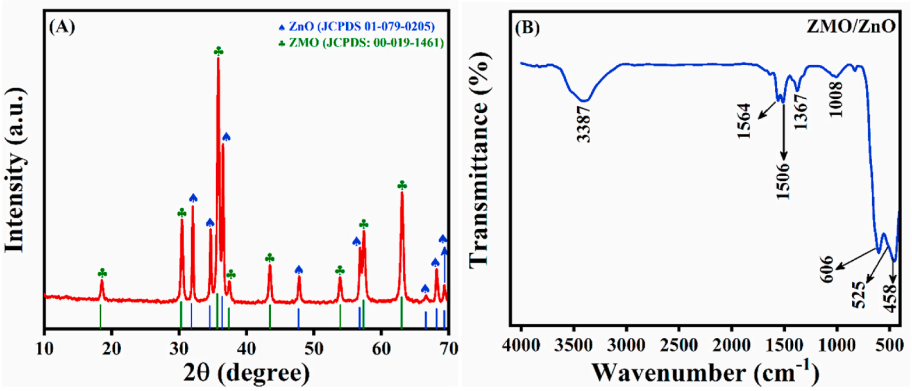

Fig. 1. P-XRD (A), FT-IR (B) spectra of ZMO/ZnO NPs.

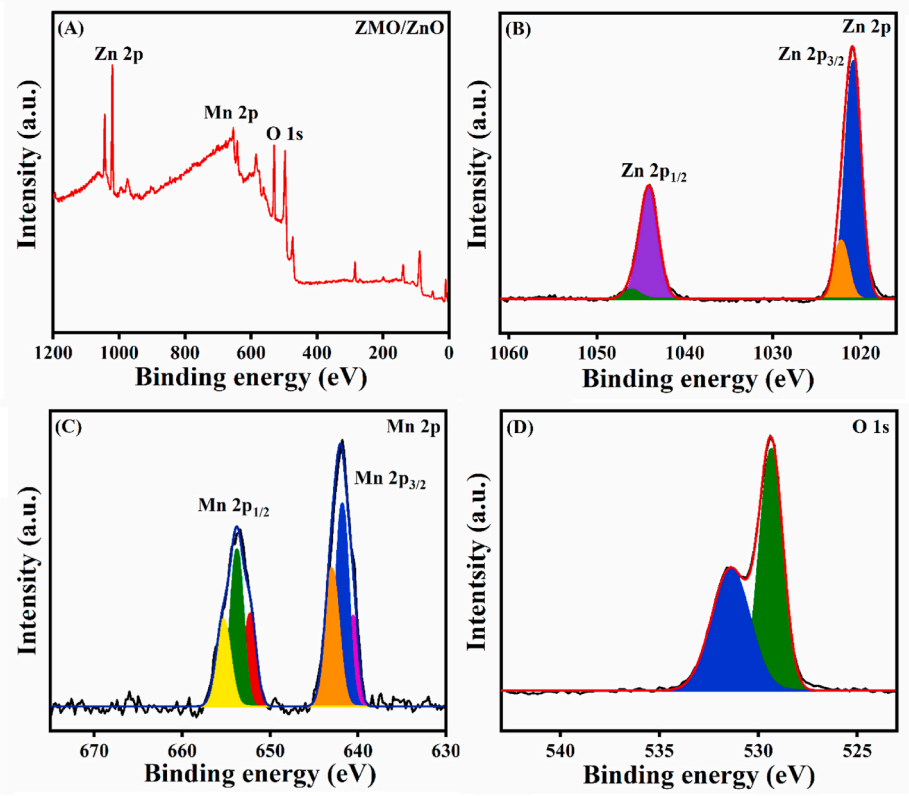

Fig. 2. XPS spectra of ZMO/ZnO NPs. (A) Survey spectrum. Core level spectra of Zn 2p (B), Mn 2p (C), and O 1s (D).

level spectrum of Zn 2p (Fig. 2B) shows two peaks that can be assigned to the presence of Zn $2p_{3/2}$ and Zn $2p_{1/2}$. The Zn 2p peaks were deconvoluted into four peaks, and the peaks at 1020.9 and 1044.1 eV correspond to the Zn^{2+} of ZMO. The peaks at 1021.9 and 1046.5 eV are associated with the Zn^{2+} in ZnO. Fig. 2C shows the spectrum of the core level of manganese 2p. The peaks at 640.5, 642.0, and 643.3 eV are related to the Mn $2p_{3/2}$ where 642.0 and 643.3 eV correspond to the Mn^{4+}, while 640.5 eV corresponds to Mn^{2+}, with a lower content [47]. Moreover, the spectrum of the core level O 1s (Fig. 2D) shows two peaks. The binding energy at 529.4 eV was assigned to the M − O bonding in the ZMO/ZnO NPs. The peak at 531.4 eV is attributed to the hydroxyl peaks at the surface of ZMO/ZnO NPs [47].

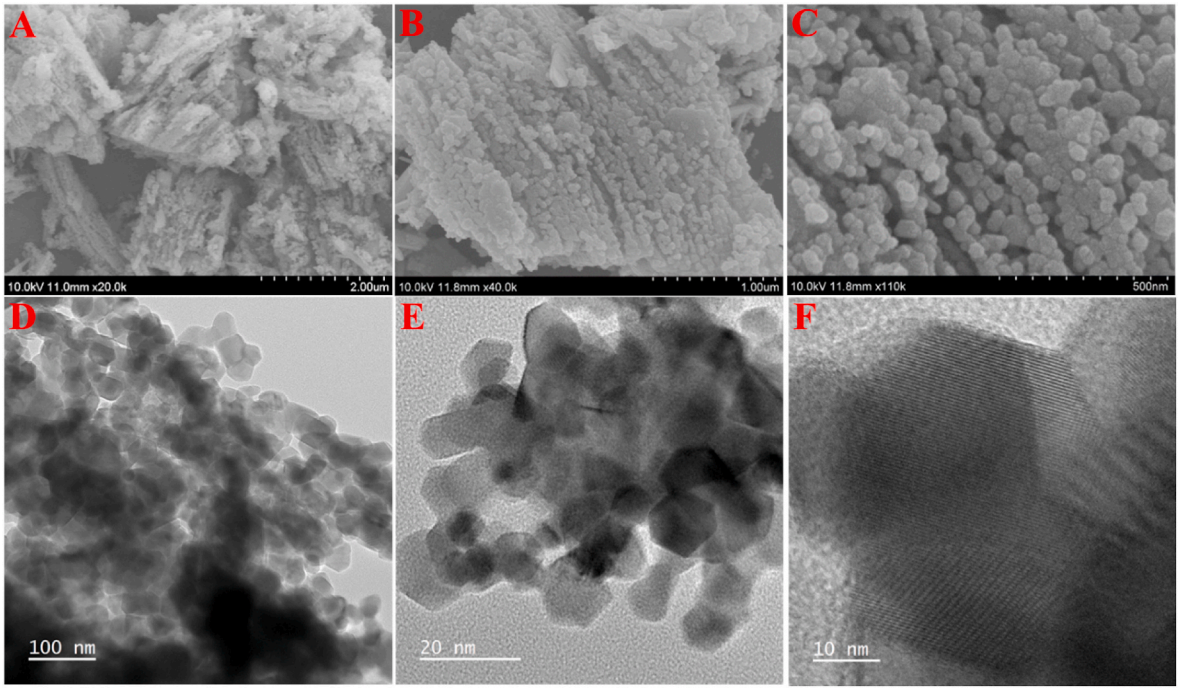

Fig. 3. (A–C) SEM images of ZMO/ZnO. (D–F) HR-TEM images of ZMO/ZnO NPs.

3.3. Morphological analysis

The SEM analysis was carried out to identify the morphology of the as-synthesized ZMO/ZnO NPs. Fig. 3(A-C) shows the SEM images (low and high magnification) of ZMO/ZnO NPs, which show the formation of an approximately spherical and hexagonal structured group of nanoparticles with an average size of 10–30 nm. From this figure, it is evident that the growth of zinc and manganese-based mixed oxide was initiated by the simple co-precipitation method. In addition to the reaction conditions (time or temperature parameters), the presence of NaOH in the precursor solution also plays an important role in determining the form of ZMO/ZnO NPs. The subsequent analysis using HR-TEM also proves the formation of ZMO/ZnO NPs. Fig. 3D, E exhibits the different magnification images of the ZMO/ZnO NPs, which are in the form of a group of nanoparticles with a size of about 10–30 nm. In addition, the magnified HR-TEM image in Fig. 3F shows the corresponding lattice fringes of the ZMO/ZnO NPs. Moreover, the elemental distribution of the ZMO/ZnO NPs was confirmed by element mapping analysis (Figs. S2A–D) and EDX (Fig. S2E). The results are shown in Fig. S2. From the corresponding figure, it can be seen that the elements such as zinc (Zn), manganese (Mn), and oxygen (O) are uniformly arranged on the surface of the ZMO/ZnO NPs. Moreover, other impurities such as Zn $(OH)_2$ or $Mn(OH)_2$ were not detected in the mapping analysis, indicating that the ZMO/ZnO NPs were successfully formed by the simple coprecipitation method.

3.4. Electrochemical characterization of ZMO/ZnO NPs

In order to analyze the electrochemical properties of bare GCE, ZnO/GCE, and ZMO/ZnO NPs/GCE, electrochemical impedance spectroscopy (EIS) was performed in 5 mM $[Fe(CN)_6]^{3-/4-}$/0.1 M KCl. The frequency was varied from 10 MHz to 100 kHz with a 5-mV sinusoidal perturbation potential. Fig. 4A shows the Nyquist plots of bare, ZnO, and ZMO/ZnO modified GCE. There is a linear relationship between the real and imaginary impedance at low frequency, indicating a diffusional process, while the semicircle at a higher frequency is related to the R_{ct} (charge transfer resistance) of the electrodes. From the Nyquist plot, the R_{ct} of the bare GCE, ZnO/GCE, and ZMO/ZnO/GCE were calculated to be 366 Ω, 1458 Ω, and 694 Ω, respectively, clearly highlighting the electrode modification with the ZnO and ZMO/ZnO NPs. The unmodified GCE electrode exhibits lower resistivity than the modified electrodes. It appears that the modified ZnO and ZMO/ZnO electrodes were impaired in conductivity due to the repulsion between the anionic $[Fe(CN)_6]^{3-/4-}$ in solution and the negatively charged metal oxides.

Fig. 4B shows the CVs of unmodified GCE, ZnO/GCE, and ZMO/ZnO/GCE cycled in 5 mM $[Fe(CN)_6]^{3-/4-}$ with 0.1 M KCl as the supporting electrolyte. The unmodified electrode shows higher peak current and lower peak-to-peak separation than the ZnO/GCE or ZnO/ZMO/GCE. On comparing the ZMO/ZnO and ZnO modifications, it is evident that higher I_{pa} and I_{pc} are obtained with the ZMO/ZnO/GCE, indicating more efficient oxidation and reduction of the $[Fe(CN)_6]^{3-/4-}$ redox couple, in good agreement with the trends seen in the EIS data. Fig. 4C shows the CV curves recorded in 5 mM $[Fe(CN)_6]^{3-/4-}$ with ZMO/ZnO/GCE at different sweep rates from 20 to 200 mV/s. From this, it can be seen that I_{pa} and I_{pc} increase linearly with increasing scan rate. Furthermore, very good linearity between I_{pc} and I_{pa} and the square root of the scan rate $(mV/s)^{1/2}$ was observed, as shown from the linear curves in Fig. 4D, indicating a diffusion-controlled process. In addition, the CVs of 5 mM $[Fe(CN)_6]^{3-/4-}$ at increasing sweep rate (20–200 mV/s) on ZnO/GCE, and the corresponding linear plots (I_{pc}, I_{pa} vs. $(\text{scan rate})^{1/2}$) are shown in Figs. S3A and B. Using the Randles-Sevcik equation (Equation (2)), the electrochemically active surface area of ZnO/GCE and ZMO/ZnO NPs/GCE were calculated using the linear plots of I_{pc}, I_{pa} vs. $(mV/s)^{1/2}$.

$$I_{pa} = (2.69 \times 10^5)\, n^{3/2}\, AC^{*}D^{1/2}\nu^{1/2} \quad (2)$$

In Equation (2), C represents the concentration of $[Fe(CN)_6]^{3-/4-}$, D represents the diffusion coefficient (7.6×10^{-6} cm^2 s^{-1}), and n depicts the number of electrons involved in the redox reaction. From Equation (2), the active surface areas of ZnO/GCE and ZMO/ZnO/GCE were calculated to be 0.06 cm^2 and 0.09 cm^2, respectively.

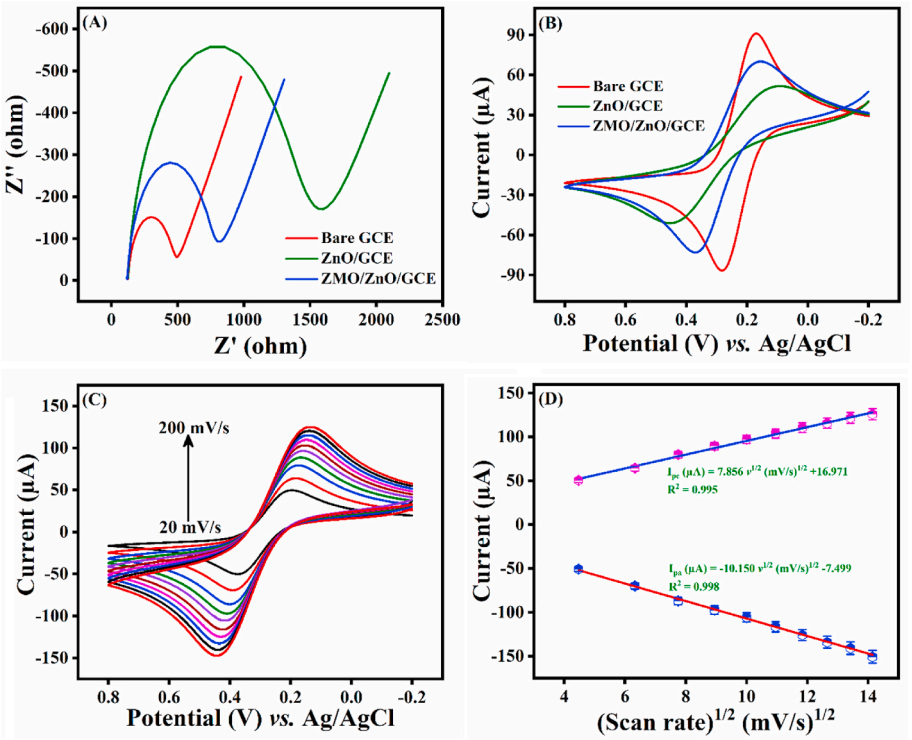

Fig. 4. (A) EIS of bare GCE, ZnO, ZMO/ZnO modified GCE. (B) CVs of 5 mM $[Fe(CN)_6]^{3-/4-}$ 0.1 M KCl at different electrodes. (C) CVs for 5 mM $[Fe(CN)_6]^{3-/4-}$ 0.1 M KCl ZMO/ZnO/GCE with various sweep rates. (D) Linear dependency between I_{pa}, I_{pc}, and $\nu^{1/2}$.

3.5. Electrochemical oxidation of CPMZ on various modified electrodes

The electrochemical oxidation of CPMZ on bare GCE, ZnO/GCE, and ZMO/ZnO/GCE was analyzed using the CV technique in 0.05 M PBS (pH 7.0). The CV experiments were performed at 50 mV/s over the potential range from −0.2 V to +1.2 V, where two oxidation waves, labelled as O_1 and O_2, can be seen, Fig. 5A. While the bare GCE can facilitate the oxidation of CPMZ (50 μM) it has the lowest peak current (I_{pa} = 1.78 μA for O_1) at 0.78 V. In contrast, a higher peak current (2.66 μA for O_1) was observed for the ZnO/GCE. This increased catalytic activity can be attributed to the presence of hydroxyl ions on the surface of the metal oxide in an aqueous medium, which may facilitate the adsorption of the target molecule and enhance the electrochemical oxidation of CPMZ [54]. The GCE modified with ZMO/ZnO shows the highest peak current (9.30 μA for O_1) with a peak potential, E_{pa} = +0.73 V. This corresponds to an approximate 50 mV shift in the peak potential to lower over-potentials, indicating a more thermodynamically favored electron transfer reaction. Fig. 5B shows the comparative bar graph of the CPMZ peak currents (I_{pa} values for O_1) at the different electrodes. From this, the GCE modified with ZMO/ZnO NPs has peak currents that are 5.22 and 3.4-times higher than the unmodified GCE and ZnO modified GCE, respectively.

This remarkable enhancement of the oxidation of CPMZ at the ZMO/ZnO NPs can be attributed to the smooth surface of the well-arranged nanoparticles and the different oxidation states of manganese. Initially, CPMZ molecules adsorb on the surface of the ZMO/ZnO NPs due to the OH^- ions in the metal oxide surface (ZMO/ZnO NPs). Then CPMZ is oxidized to $CPMZ^{\bullet+}$ with the reduction of Mn^{4+} to the corresponding lower oxidation states, such as Mn^{3+} and Mn^{2+} [55].

For the oxidation of CPMZ at the modified electrodes, anodic and cathodic waves are evident, with all electrodes showing two oxidation peaks at a potential of about 0.6–1.1 V (Fig. 5A). The first oxidation wave (O_1) occurs as the nitrogen atom of CPMZ is oxidized to generate the cationic radical product $CPMZ^{\bullet+}$. Next, the sulfur atom of $CPMZ^{\bullet+}$ is oxidized to generate another cationic radical, and this gives rise to the peak at O_2. In the reverse direction, a cathodic peak is obtained, *i.e.*, a quasi-reversible process of the first electrochemical oxidation (R_1) takes place at the nitrogen atom. Another cathodic peak, R_2, was obtained when the electrode was modified with ZMO/ZnO/GCE. The emergence of this R_2 wave can be explained in terms of a chemical process where the adsorbed OH^- ions combine with the electron-deficient sulfur atom to form the sulfoxide of CPMZ [56,57]. The overall electrochemical oxidation of CPMZ on ZMO/ZnO/GCE is summarized in Scheme 2.

Clearly, the efficacious electrochemical interaction between the active surface of synergistically refashioned ZMO/ZnO NPs/GCE and the functional atoms (nitrogen and sulfur atom) of CPMZ result in excellent electrocatalytic activity. Hence, the ZMO/ZnO nanoparticles are an excellent and active material for the electrocatalytic determination of CPMZ due to their superior electrical conductivity and eco-friendly nature (non-toxic). Furthermore, the ZMO/ZnO nanoparticles contain abundant vacant sites that can promote the electron transfer between the highest occupied molecular orbital of CPMZ and the ZMO/ZnO nanoparticles, with susceptible active sites for the corresponding oxidation process.

3.6. Concentration effect of CPMZ on ZMO/ZnO/GCE

The electrocatalytic activity of ZMO/ZnO/GCE was further analyzed with various concentrations of CPMZ in 0.05 M PBS (pH 7.0). Fig. 5C shows the CV curves of CPMZ with different concentrations from 100 to 350 μM at a sweep rate of 50 mV/s. From this, it can be seen that the I_{pa} increases during the stepwise addition of CPMZ, oxidation current response was linearly enhanced with respect to the CPMZ concentration. Interestingly, the oxidation current response of CPMZ was linearly correlated to the concentration of CPMZ, and the obtained linear plot was portrayed in Fig. 5D with the correlation coefficient of I_{pa} (μA) = 0.036*C* (μM) + 10.124 (R^2 = 0.979). These obtained results show that the ZMO/ZnO/GCE has excellent electrocatalytic performance for the oxidation of CPMZ. This is due to the synergetic effect between the mixed-metal oxides and the higher oxidation state of manganese.

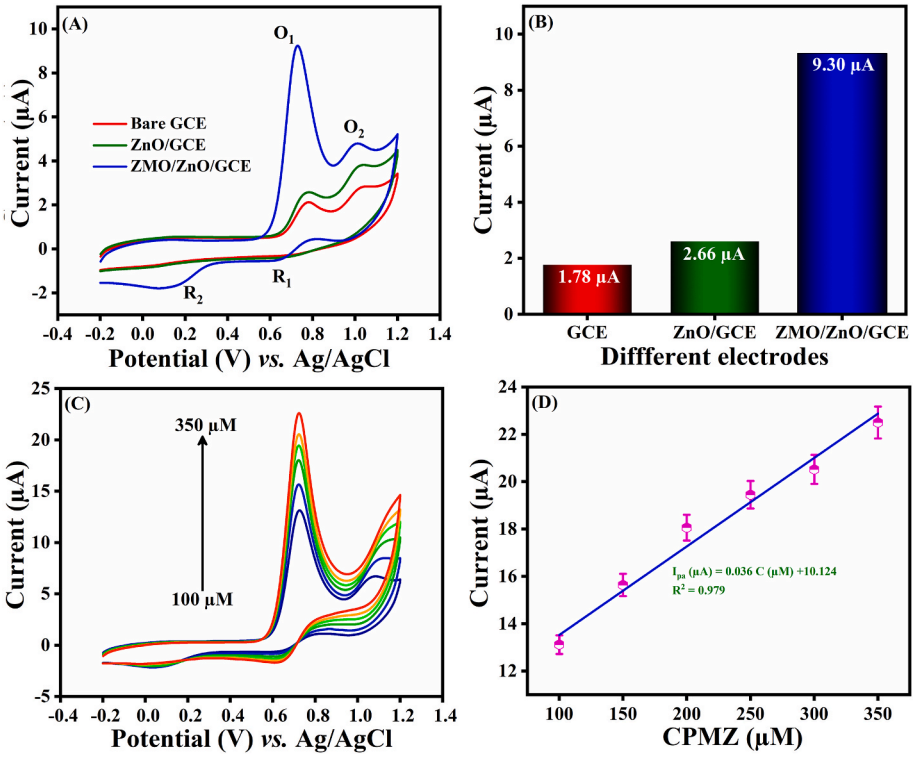

Fig. 5. (A) CV responses of 50 μM CPMZ at different electrodes such as bare GCE, ZnO/GCE, ZMO/ZnO/GCE. (B) Bar graph: Anodic current of 50 μM CPMZ on unmodified, modified GCE. (C) CV curves of the different concentrations of CPMZ from 100 μM to 350 μM at ZMO/ZnO/GCE. (D) Linear plot: different concentrations of CPMZ versus the resulting oxidation peak current at ZMO/ZnO/GCE. In all electrochemical studies, N_2 saturated 0.05 M PBS (pH 7.0) acted as the supporting electrolyte. All electrochemical experiments were conducted at a 50 mV/s sweep rate.

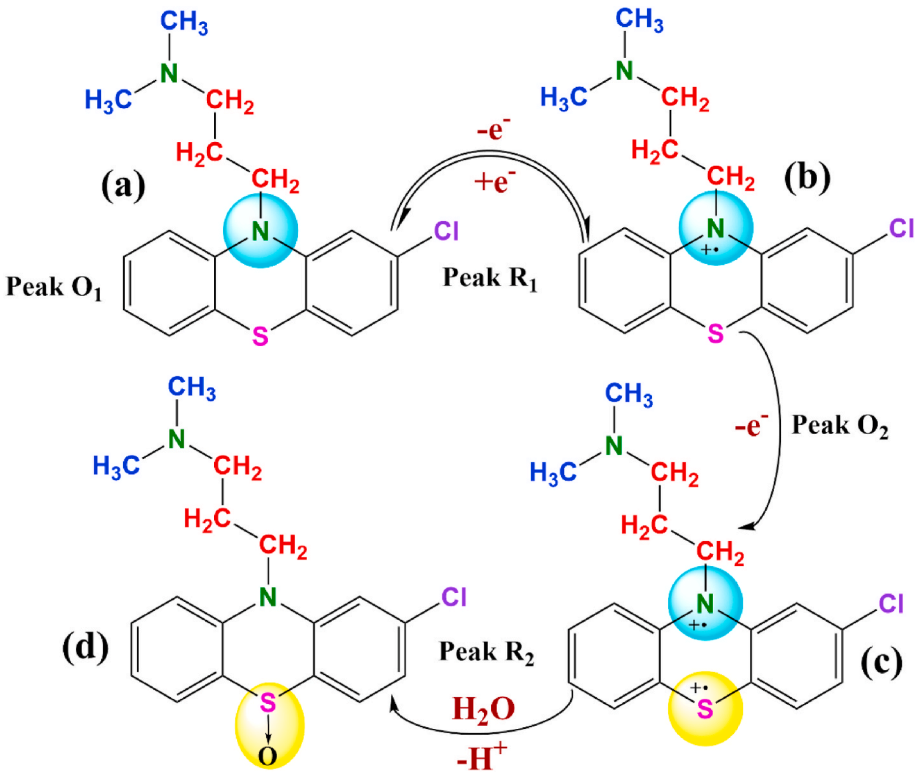

Scheme 2. Possible electrochemical oxidation mechanisms of CPMZ at an electrode modified with ZMO/ZnO NPs.

3.7. pH optimization

Protons can affect the peak potential and peak current of electrochemical reactions. Therefore, optimizing the electrolyte pH is a required parameter for the electrochemical determination of CPMZ.

The CV was carried out with various pH values (0.05 M PBS) on

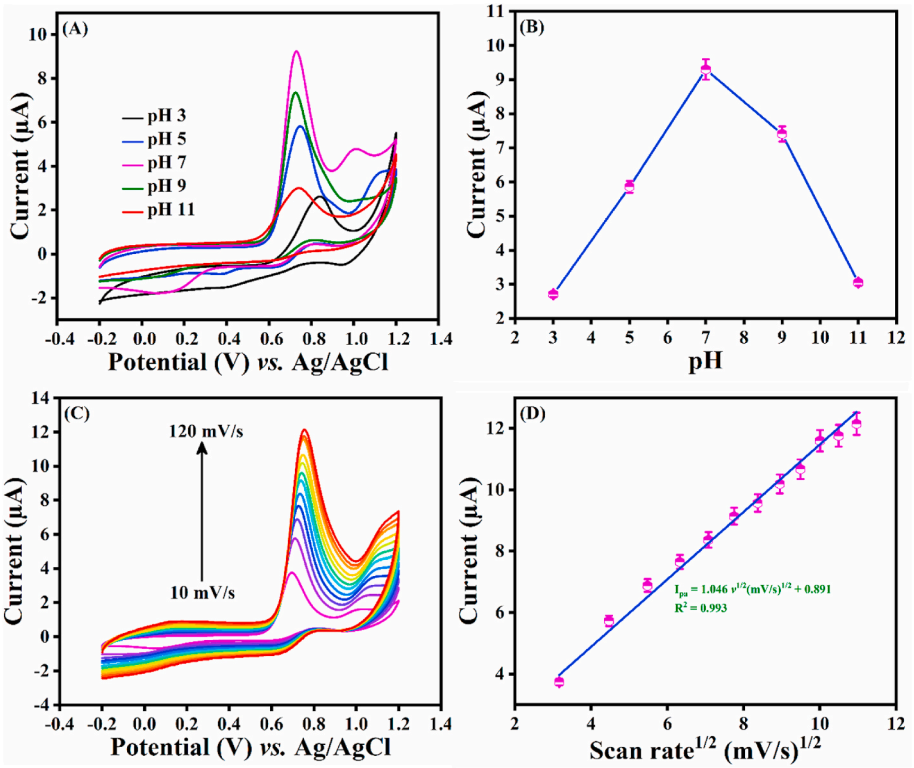

Fig. 6. (A) CV responses of 50 µM CPMZ on ZMO/ZnO/GCE in 0.05 M PB solution at different pH values such as pH = 3.0, 5.0, 7.0, 9.0, and 11.0 (scan rate 50 mV/s). (B) Comparison plot: resulting current response of 50 µM CPMZ on ZMO/ZnO/GCE with different pH solutions. (C) CV curves of 50 µM CPMZ on ZMO/ZnO/GCE at different scan rates from 10 to 120 mV/s (Supporting electrolyte: N_2 saturated 0.05 M PBS (pH 7.0)). (D) Linear plot: I_{pa} with respect to the square root of scan rate.

ZMO/ZnO/GCE for 50 μM CPMZ. Fig. 6A shows the CVs recorded with ZMO/ZnO/GCE in 0.05 M PBS with different pH (3.0–11.0). Apart from the more acidic solution at a pH of 3.0, the peak potentials remain essentially constant from pH values of 5–13. However, the I_{pa} is increased when the pH is raised from 3.0 to 7.0. In contrast, the I_{pa} decreases when the pH is above 7.0. Fig. 6B shows the relationship between the I_{pa} of CPMZ and the pH. The highest anodic peak current is obtained at pH 7.0, and this was chosen as the optimum electrolyte pH for further electrochemical studies. It is also evident from Fig. 6A that the redox behavior corresponding to the conversion of $CMPZ^{\bullet+}$ to CPMZ becomes evident at a pH of 3.0. A more pronounced reduction wave is observed at about 1.0 V, indicating that protons facilitate this reduction process. This wave is diminished as the pH is increased, and an irreversible oxidation of CMPZ is observed at pH 11.0. Therefore, it can be concluded that the electrocatalytic oxidation of CPMZ is a quasi-reversible process in acidic media and an irreversible process in basic media.

3.8. Scan rate studies

The reaction kinetics of CPMZ on ZMO/ZnO/GCE were analyzed using scan rate studies. Fig. 6C shows the CVs of 50 μM CPMZ with different sweep rates (10–120 mV/s). It can be seen that the peak current increases with increasing sweep rate, and the peak potential is shifted positively. Also, a linear relationship was found between the anodic peak current and the square root of the sweep rate. Fig. 6D shows the linear plot between the CPMZ peak current and the square root of the sweep rate with the linear regression equation I_{pa} (μA) = 1.046 $\nu^{1/2}$ $(mV/s)^{1/2}$ + 0.891 and the correlation coefficient is R^2 = 0.993. This indicates that the electrochemical oxidation of CPMZ on ZMO/ZnO/GCE is a diffusion-controlled process. In other words, the reaction rate depends on the CPMZ molecules diffusing first to the subsurface and then to the interface. Moreover, the slope (Fig. S4A) between log I_{pa} and log scan rate (ν) (0.45) agrees very well with the theoretical value of 0.5 for diffusion control. The electron transfer coefficient (α) of the irreversible electrochemical reaction can be calculated using the equation of Bard and Faulkner [58],

$$E_p - E_{p1/2} = 47.7/\alpha \quad (3)$$

where E_p is the peak potential and $E_{p1/2}$ is the half-wave potential. From this, α can be calculated as 0.76. Using the computed α value, the diffusion coefficient can be estimated using Equation (4) [59], and the slope obtained from the linear plot between the peak current (I_{pa}) and the square root of the scan rate $(mV/s).^{1/2}$

$$I_p = (2.99 \times 10^5)\, n\alpha^{1/2} AC^* D^{1/2} \nu^{1/2} \quad (4)$$

Here n is the number of electrons transferred in the electrochemical reaction (n = 1), α is the electron transfer coefficient (α = 0.76), A represents the surface area of ZMO/ZnO/GCE (0.09 cm^2), C* is the concentration of CPMZ (5×10^{-5} mol/L) and $\nu^{1/2}$ corresponds with the square root of scan rate, and D is the diffusion coefficient of CPMZ, which can be calculated as 3.5×10^{-3} cm^2 s^{-1}.

According to Bard and Faulkner, equation (5) [59], can be used to compute the rate constant. In this analysis, n, F, A, and C* have their usual meanings, a number of electrons (n = 1), Faraday's constant (F = 96485.3), the surface area and concentration of CPMZ ($C^* = 5 \times 10^{-5}$ mol/L). E^0 is the formal potential obtained by extrapolating the linear plot (Fig. S4B) of the log scan rate *vs.* E_{pa} to $\nu = 0$.

$$I_p = 0.227\, n\, F\, A\, C^*\, K^0 \exp\left[-\alpha nF/RT\,(E_p - E^0)\right] \quad (5)$$

Fig. S4C shows the linear plot obtained between ln I_{pa} and E_p-E_0 along with the linear regression equation, ln I_{pa} (μA) = 18.777 (E_{pa}-E_0) +1.26 (R^2 = 0.987). From the linear regression equation, K^0 is related to the observed intercept of this equation. Based on equation (5), the heterogeneous rate constant (K^0) was calculated as 2.2×10^{-2} cm/s.

3.9. Determination of CPMZ on ZMO/ZnO/GCE

Analytical parameters such as linear range, detection limit (LOD), sensitivity, and selectivity of ZMO/ZnO/GCE were evaluated using the DPV technique as it has higher sensitivity and better resolution than the CV technique. DPV was performed for the various concentrations of CPMZ (0.05–1626 μM) in 0.05 M PBS (pH 7.0) in the potential range of +0.2 V to +1.0 V. As shown in Fig. 7A, CPMZ at the lowest concentration of 0.05 μM showed a DPV current at +0.70 V. Moreover, the I_{pa} increased directly with the CPMZ concentration. The dependence of CPMZ concentration on I_{pa} was plotted from 0.05 to 125.55 μM and 185.55–1625 μM along with the linear regression equations which were obtained as I_{pa} (μA) = 0.051 C (μM) + 0.915 (R^2 = 0.978) and I_{pa} (μA) = 0.017 (μM) C + 5.520 (R^2 = 0.996) (Fig. 7B). These two linear ranges may be due to the fouling effect, which means that CPMZ was easily oxidized at the ZMO/ZnO/GCE at low concentrations. However; some of the oxidized products accumulate at the electrode and inhibit further oxidation at higher concentrations. In this analysis, the analytical properties such as LOD, sensitivity were calculated based on the first linear range of 0.05–125.55 μM. According to the IUPAC convention, equation in (6) Q denotes the standard deviation resulting from the blank signal at ZMO/ZnO/GCE, and S is the slope resulting from the linear equation.

$$LOD = 3Q/S \quad (6)$$

On this basis, LOD was calculated to be 0.019 μM, and the sensitivity of the ZMO/ZnO/GCE is 0.760 μA μM^{-1} cm^{-2}. These obtained analytical values were compared with previously published results and are summarized in Table 1. Based on this comparison, it is evident that the ZMO/ZnO/GCE has a wide linear range, low LOD value, and excellent sensitivity compared to the previously modified electrodes. These impressive electroanalytical results can be traced to the synergistic effect of the two metal oxides (ZMO/ZnO NPs), with the differential oxidation of manganese enabling the superior electrocatalytic activity in the determination of CPMZ.

3.10. Selectivity, repeatability, and stability studies of ZMO/ZnO/GCE the CPMZ

Selectivity is essential for an electrochemical sensor. Fig. 8A shows the DPV responses of 40 μM CPMZ along with a 3-fold higher concentration of interfering compounds, namely, glucose (GLU), lactose (LAC), K^+, Cl^-, Na^+, uric acid (UA), and ascorbic acid (AA). The interferences show a maximum error of ±5% in the peak current of CPMZ. Fig. 8B shows the interference study of ZMO/ZnO/GCE with 40 μM CPMZ along with equal concentrations of co interfering compounds such as quercetin (QC), paracetamol (PARA), promethazine (PMZ), and thioridazine (THZ), and again, these exhibit little interference, with a maximum deviation of ±4% in the peak current of CPMZ.

Moreover, Figs. S5A and B show the bar diagram which compares the CPMZ anodic peak current with the current obtained in the presence of the GLU, LAC, AA, UA, Na^+, K^+, Cl^- (Fig. S5A), and QC, PARA, PMZ, and THZ (Fig. S5B) interferences. Figs. S5A and B demonstrate that the maximum deviation in the peak current of CPMZ is less than ±1 μA in the presence of the interferences. In conclusion, the ZMO/ZnO/GCE has a satisfactory selectivity towards the determination of CPMZ.

Fig. 8C shows the repeatability study of ZMO/ZnO/GCE exhibiting 10 successive DPV curves for the 30 μM CPMZ, which show less than a ±5% reduction in the current compared with the initial current. In addition, stability studies were analyzed over 10 days. For this study, the fabricated ZMO/ZnO NPs/GCE was stored and removed at 2-day intervals and tested to detect CPMZ. Fig. 8D exhibits the DPV curves of 30 μM CPMZ in the stability studies and again demonstrates that the changes in I_{pa} are less than ±5% from the freshly prepared ZMO/ZnO NPs/GCE. These results demonstrate that ZMO/ZnO/GCE shows good

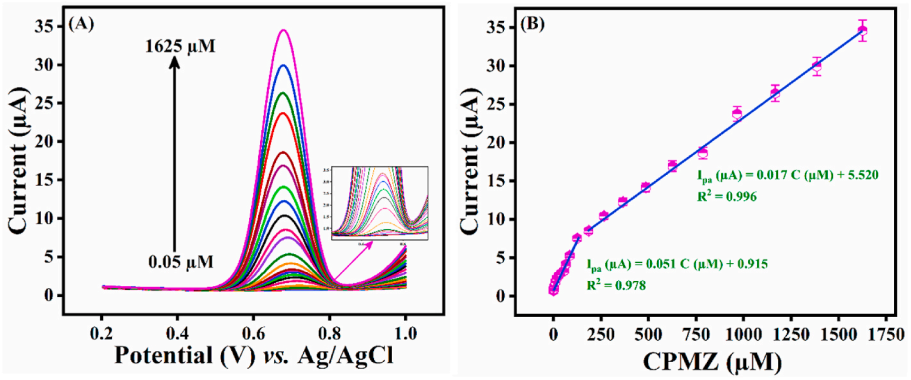

Fig. 7. (A) DPV responses of successive addition of different concentrations (0.05 µM–1625 µM) of CPMZ to ZMO/ZnO/GCE in the potential range from 0.2 to 1.0 V. (B) Linear ranges: Concentration of CPMZ versus the resulting oxidation peak current.

Table 1
Comparison of various modified electrodes for CPMZ determination.

Electrode	Method	Linear range (µM/L)	LOD (µM/L)	Reference
P3MT/γ-CD	SWV	0.5–50	2	[60]
N-CDs/Cu_2O	DPV	0.001–230	0.025	[8]
La^{3+}/Co_3O_4/GCE	DPV	0.5–400	0.08	[61]
CdO NPs/IL/CPE	SWV	0.1–350	0.07	[62]
ZMO/ZnO/GCE	DPV	0.05–125.55 185.55–1625	0.019	This work

selectivity, excellent repeatability, and stability.

3.11. Determination of CPMZ in real sample

To explore the practical application of ZMO/ZnO NPs/GCE, the DPV was carried out in real samples such as human blood serum and urine samples (prepared according to section 2.4) with the successive addition of CPMZ from 5 to 15 µM in 0.05 M PBS (pH 7.0). Fig. 9A and B show the DPV curves performed in the real sample analysis, and corresponding recovery results are listed in Table S1. This analysis in the human urine and blood serum samples signify that ZMO/ZnO NPs modified GCE has a sufficient sensing capability for the CPMZ determination in real sample analysis.

4. Conclusion

In summary, cubic $ZnMnO_3$ and hexagonal ZnO heterostructure nanoparticles (ZMO/ZnO NPs) were prepared by a co-precipitation method. Based on ZMO/ZnO NPs, an electrochemical sensor for CPMZ was constructed. ZMO/ZnO NPs/GCE showed a better current response

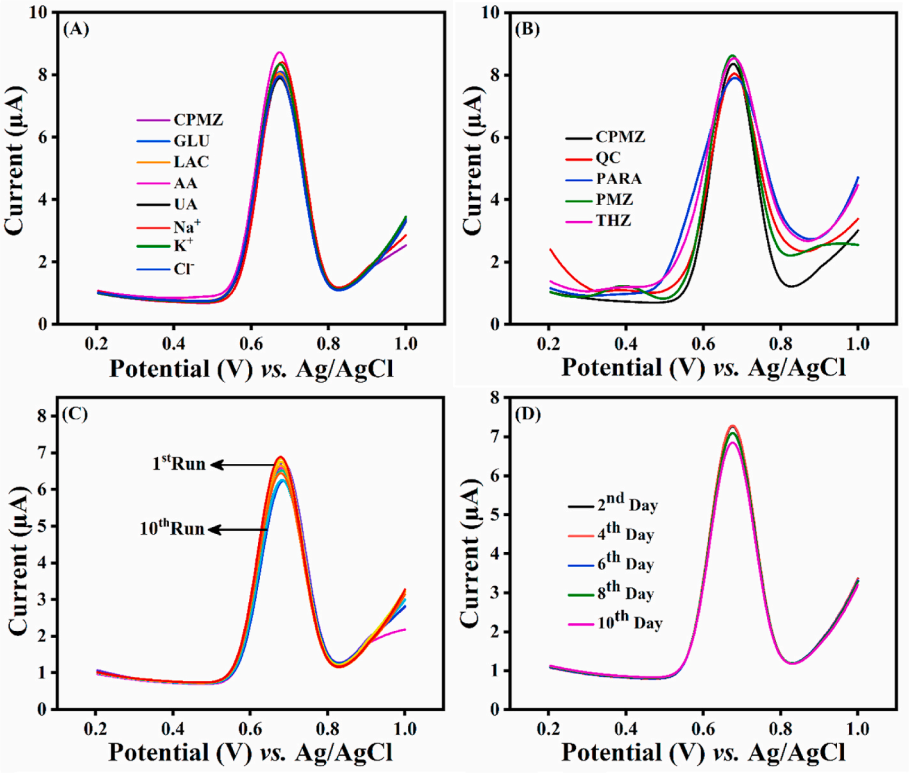

Fig. 8. (A) DPV curves of 40 µM of CPMZ and interferences, namely GLU, LAC, AA, UA, Na^+, K^+, and Cl^-. (B) DPV results of 40 µM of CPMZ coexistence with some potentially interfering drugs such as PARA, PMZ, THZ, and a flavonoid QC over the surface of ZMO/ZnO/GCE. (C) DPV curves of repeatability test towards the CPMZ (30 µM) detection for 10 consecutive measurements. (D) DPV curves of storage stability test with 30 µM of CPMZ at ZMO/ZnO/GCE.

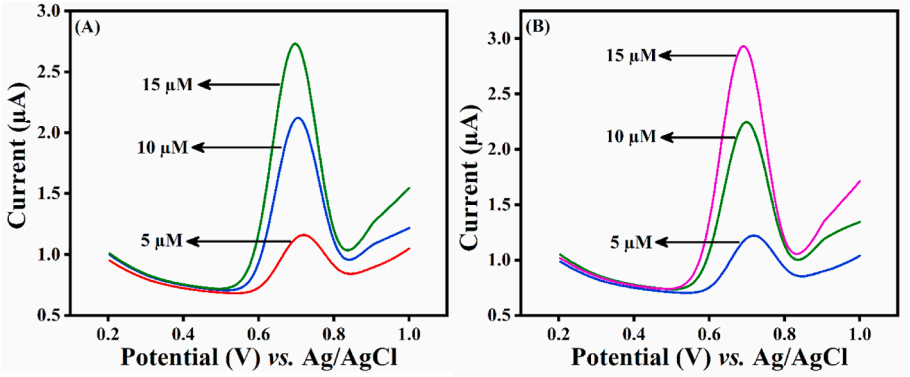

Fig. 9. DPV curves of real sample analysis of CPMZ at ZMO/ZnO/GCE (A) Human urine (B) Blood serum.

than bare GCE. This improved electrocatalytic activity can be attributed to the aggregation of the nanoparticles with smooth surface, the multivalence of manganese, and a synergistic effect of the hetero-structure. The electrochemical determination of CPMZ on ZMO/ZnO NPs/GCE showed good sensitivity (0.760 μA μM^{-1} cm^{-2}), LOD (0.019 μM) and two linear ranges (0.05–125.55 μM and 185.55–1625 μM). In addition, the developed CPMZ sensor has reasonable repeatability, storage stability, and selectivity. Moreover, the analysis of real samples in biological fluids (human urine, blood serum) was performed and showed acceptable recovery.

CRediT authorship contribution statement

Karuppaiah Balamurugan: Conceptualization, Experimental operation, Data curation, Analysis, Writing – original draft. **Raj Karthik:** Investigation, Validation, Data curation, Analysis. **Shen-Ming Chen:** Supervision, Investigation, Funding acquisition, Formal analysis, Writing – review & editing. **Ramaraj Sukanya:** Writing – review & editing, Software, Formal analysis, Writing – original draft. **Bhuvaneswari Thasma Subramanian:** Writing – review & editing, Software, Formal analysis, Writing – original draft. **Valsala Madhavan Nair Biju:** Supervision, Investigation, Writing – review & editing. **Jae-Jin Shim:** Supervision, Investigation, Funding acquisition, Formal analysis, Writing – review & editing. **Carmel B. Breslin:** Supervision, Investigation, Writing – review & editing.

Declaration of competing interest

The authors declare that they have no known competing financial interests or personal relationships that could have appeared to influence the work reported in this paper.

Acknowledgments

The authors acknowledge the Ministry of Science and Technology (MOST 110-2113-M-027-003). This study was supported by Science Foundation Ireland under grant number SFI/20/FFP-P/8793 and the National Research Foundation (NRF) of the Republic of Korea under the frameworks of the Priority Research Centers Program (NRF-2014R1A6A1031189) and the Regional University Superior Scientist Research Program (NRF-2020R1I1A3073981) funded by the Ministry of Education, the Republic of Korea.

Appendix A. Supplementary data

Supplementary data to this article can be found online at https://doi.org/10.1016/j.compositesb.2022.109822.

References

[1] Kumar JV, Karthik R, Chen SM, Kokulnathan T, Sakthinathan S, Muthuraj V, et al. Highly selective electrochemical detection of antipsychotic drug chlorpromazine in drug and human urine samples based on peas-like strontium molybdate as an electrocatalyst. Inorg Chem Front 2018;5:643–55. https://doi.org/10.1039/c7qi00743d.

[2] Purushothama HT, Nayaka YA, Vinay MM, Manjunatha P, Yathisha RO, Basavarajappa KV. Pencil graphite electrode as an electrochemical sensor for the voltammetric determination of chlorpromazine. J Sci Adv Mater Devices 2018;3:161–6. https://doi.org/10.1016/j.jsamd.2018.03.007.

[3] Kaleeswarran P, Sriram B, Wang SF, Baby JN, Arumugam A, Bilgrami AL, et al. Electrochemical detection of antipsychotic drug in water samples based on nano/sub-microrod-like $CuBi_{2-x}In_xO_4$ electrocatalysts. Microchem J 2021;163:105886. https://doi.org/10.1016/j.microc.2020.105886.

[4] Karpińska J. The use of internal standard method for derivative-spectrophotometric determination of chlorpromazine hydrochloride. Anal Lett 2000;33:1555–66. https://doi.org/10.1080/00032710008543143.

[5] Zhang L, Wu P, Zhang Y, Jin Q, Yang D, Wang L, et al. A GC/MS method for the simultaneous determination and quantification of chlorpromazine and diazepam in pork samples. Anal Methods 2014;6:503–8. https://doi.org/10.1039/c3ay41130c.

[6] Stevenson D, Reid E. Determination of chlorpromazine and its sulfoxide and 7-hydroxy metabolites by ion-pair high pressure liquid chromatography. Anal Lett 1981;14:741–61. https://doi.org/10.1080/00032718108055479.

[7] Xu G, Dong S. Electrochemiluminescent detection of chlorpromazine by selective preconcentration at a lauric acid-modified carbon paste electrode using tris(2,2'-bipyridine)ruthenium(II). Anal Chem 2000;72:5308–12. https://doi.org/10.1021/ac000507s.

[8] Palakollu VN, Karpoormath R, Wang L, Tang JN, Liu C. A versatile and ultrasensitive electrochemical sensing platform for detection of chlorpromazine based on nitrogen-doped carbon dots/cuprous oxide composite. Nanomaterials 2020;10:1–15. https://doi.org/10.3390/nano10081513.

[9] Parvin MH, Golivand MB, Najafi M, Shariaty SM. Carbon paste electrode modified with cobalt nanoparticles and its application to the electrocatalytic determination of chlorpromazine. J Electroanal Chem 2012;683:31–6. https://doi.org/10.1016/j.jelechem.2012.07.018.

[10] Karimi-Maleh H, Karimi F, Fu L, Sanati AL, Alizadeh M, Karaman C, et al. Cyanazine herbicide monitoring as a hazardous substance by a DNA nanostructure biosensor. J Hazard Mater 2022;423. https://doi.org/10.1016/j.jhazmat.2021.127058.

[11] Karimi-Maleh H, Khataee A, Karimi F, Baghayeri M, Fu L, Rouhi J, et al. A green and sensitive guanine-based DNA biosensor for idarubicin anticancer monitoring in biological samples: a simple and fast strategy for control of health quality in chemotherapy procedure confirmed by docking investigation. Chemosphere 2022;291:1–8. https://doi.org/10.1016/j.chemosphere.2021.132928.

[12] Hsu FH, Hsu SY, Pao CW, Chen JL, Chen CL, Chen JM, et al. Electrochemical properties and mechanism of $CoMoO_4$@$NiWO_4$ core-shell nanoplates for high-performance supercapacitor electrode application studied: via in situ X-ray absorption spectroscopy. Nanoscale 2020;12:13388–97. https://doi.org/10.1039/d0nr00349b.

[13] Ameri B, Davarani SSH, Moazami HR, Darjazi H. Cathodic electrosynthesis of $ZnMn_2O_4$/Mn_3O_4 composite nanostructures for high performance supercapacitor applications. J Alloys Compd 2017;720:408–16. https://doi.org/10.1016/j.jallcom.2017.05.271.

[14] Saravanakumar B, Muthu Lakshmi S, Ravi G, Ganesh V, Sakunthala A, Yuvakkumar R. Electrochemical properties of rice-like copper manganese oxide ($CuMn_2O_4$) nanoparticles for pseudocapacitor applications. J Alloys Compd 2017;723:115–22. https://doi.org/10.1016/j.jallcom.2017.06.249.

[15] Umar A, Akhtar MS, Ameen S, Imran M, Kumar R, Wang Y, et al. Colloidal synthesis of $NiMn_2O_4$ nanodisks decorated reduced graphene oxide for electrochemical applications. Microchem J 2021;160:105630. https://doi.org/10.1016/j.microc.2020.105630.

[16] Liu W, Zhou Z, Yin L, Zhu Y, Zhao J, Zhu B, et al. A novel self-powered bioelectrochemical sensor based on $CoMn_2O_4$ nanoparticle modified cathode for

sensitive and rapid detection of hydrogen peroxide. Sensors Actuators, B Chem 2018;271:247–55. https://doi.org/10.1016/j.snb.2018.05.070.
[17] Rahman MM. Efficient formaldehyde sensor development based on Cu-codoped ZnO nanomaterial by an electrochemical approach. Sensors Actuators, B Chem 2020;305:127541. https://doi.org/10.1016/j.snb.2019.127541.
[18] Alam MM, Uddin MT, Asiri AM, Awual MR, Fazal MA, Rahman MM, et al. Fabrication of selective L-glutamic acid sensor in electrochemical technique from wet-chemically prepared RuO_2 doped ZnO nanoparticles. Mater Chem Phys 2020; 251:123029. https://doi.org/10.1016/j.matchemphys.2020.123029.
[19] Shetti NP, Malode SJ, Nayak DS, Bagihalli GB, Kalanur SS, Malladi RS, et al. Fabrication of ZnO nanoparticles modified sensor for electrochemical oxidation of methdilazine. Appl Surf Sci 2019;496:143656. https://doi.org/10.1016/j.apsusc.2019.143656.
[20] Hameed S, Khalil AT, Ali M, Numan M, Khamlich S, Shinwari ZK, et al. Greener synthesis of ZnO and Ag-ZnO nanoparticles using Silybum marianum for diverse biomedical applications. Nanomedicine 2019;14:655–73. https://doi.org/10.2217/nnm-2018-0279.
[21] Nwanya AC, Deshmukh PR, Osuji RU, Maaza M, Lokhande CD, Ezema FI. Synthesis, characterization and gas-sensing properties of SILAR deposited ZnO-CdO nano-composite thin film. Sensors Actuators, B Chem 2015;206:671–8. https://doi.org/10.1016/j.snb.2014.09.111.
[22] Ngom BD, Mpahane T, Manikandan E, Maaza M. ZnO nano-discs by lyophilization process: size effects on their intrinsic luminescence. J Alloys Compd 2016;656: 758–63. https://doi.org/10.1016/j.jallcom.2015.09.230.
[23] Li F, Ni B, Zheng Y, Huang Y, Li G. A simple and efficient voltammetric sensor for dopamine determination based on ZnO nanorods/electro-reduced graphene oxide composite. Surfaces and Interfaces 2021;26:101375. https://doi.org/10.1016/j.surfin.2021.101375.
[24] Sebastian N, Yu WC, Hu YC, Balram D, Yu YH. Sonochemical synthesis of iron-graphene oxide/honeycomb-like ZnO ternary nanohybrids for sensitive electrochemical detection of antipsychotic drug chlorpromazine. Ultrason Sonochem 2019;59:104696. https://doi.org/10.1016/j.ultsonch.2019.104696.
[25] Si X, Wei Y, Wang C, Li L, Ding Y. A sensitive electrochemical sensor for ofloxacin based on a graphene/zinc oxide composite film. Anal Methods 2018;10:1961. https://doi.org/10.1039/c8ay00127h. –7.
[26] Morán-Lázaro JP, Guillen-López ES, López-Urias F, Muñoz-Sandoval E, Blanco-Alonso O, Guillén-Bonilla H, et al. Synthesis of znmn2 o4 nanoparticles by a microwave-assisted colloidal method and their evaluation as a gas sensor of propane and carbon monoxide. Sensors (Switzerland) 2018;18. https://doi.org/10.3390/s18030701.
[27] Li Y, Huan K, Deng D, Tang L, Wang J, Luo L. Facile synthesis of $ZnMn_2O_4$@rGO microspheres for ultrasensitive electrochemical detection of hydrogen peroxide from human breast cancer cells. ACS Appl Mater Interfaces 2020;12:3430–7. https://doi.org/10.1021/acsami.9b19126.
[28] Guillemet-Fritsch S, Chanel C, Sarrias J, Bayonne S, Rousset A, Alcobe X, et al. Structure, thermal stability and electrical properties of zinc manganites. Solid State Ionics 2000;128:233–42. https://doi.org/10.1016/S0167-2738(99)00340-9.
[29] Guan Y, Feng Y, Mu Y, Fang L, Zhang H, Wang Y. Ultra-tiny $ZnMn_2O_4$ nanoparticles encapsulated in sandwich-like carbon nanosheets for high-performance supercapacitors. Nanotechnology 2016;27. https://doi.org/10.1088/0957-4484/27/47/475402.
[30] Jaćimović J, Micković Z, Gaál R, Smajda R, Váju C, Sienkiewicz A, et al. Synthesis, electrical resistivity, thermo-electric power and magnetization of cubic $ZnMnO_3$. Solid State Commun 2011;151:487–90. https://doi.org/10.1016/j.ssc.2010.12.025.
[31] Rall JD, Thota S, Kumar J, Seehra MS. Synthesis, structure, and magnetic behavior of nanoparticles of cubic $ZnMnO_3$. Appl Phys Lett 2012;100:1–5. https://doi.org/10.1063/1.4729817.
[32] Ekhande LV, Dhas VV, Kolekar YD, Ghosh K, Date SK, Patil SI. Role of defects in enhancing room temperature ferromagnetism of Mn doped ZnO nanoparticles. Phys Status Solidi Basic Res 2013;250:1389–97. https://doi.org/10.1002/pssb.201248567.
[33] Zhang X, Wen L, Xu Y, Sun K, Hao X. Magnetic interactions in $ZnMnO_3$: active role of Zn $3d^{10}$ orbitals, in comparison with $MgMnO_3$. Inorg Chem 2020;59:16205–14. https://doi.org/10.1021/acs.inorgchem.0c01869.
[34] Liu X, Zhao C, Zhang H, Shen Q. Facile synthesis of porous $ZnMnO_3$ spherulites with a high lithium storage capability. Electrochim Acta 2015;151:56–62. https://doi.org/10.1016/j.electacta.2014.11.020.
[35] Geng F, Yuan A, Xu J. Synthesis and electrochemical performance of a coaxial VGCF@$ZnMnO_3$ nanocomposite as a high-capacity anode material for lithium-ion batteries. Electrochim Acta 2016;216:376–85. https://doi.org/10.1016/j.electacta.2016.09.055.
[36] Peng L, Dong S, An Y, Qu M. Controllable generation of ZnO/$ZnCo_2O_4$ arising from bimetal-organic frameworks for electrochemical detection of naphthol isomers. Analyst 2021;146:3352–60. https://doi.org/10.1039/d1an00193k.
[37] Balamurugan K, Rajakumaran R, Chen SM, Karthik R, Shim JJ, Shafi PM. Massive engineering of spinel cobalt tin oxide/tin oxide-based electrocatalyst for the selective voltammetric determination of antibiotic drug furaltadone in water samples. J Alloys Compd 2021;882:160750. https://doi.org/10.1016/j.jallcom.2021.160750.
[38] Karimi-Maleh H, Orooji Y, Karimi F, Alizadeh M, Baghayeri M, Rouhi J, et al. A critical review on the use of potentiometric based biosensors for biomarkers detection. Biosens Bioelectron 2021:184. https://doi.org/10.1016/j.bios.2021.113252.
[39] Karimi-Maleh H, Yola ML, Atar N, Orooji Y, Karimi F, Senthil Kumar P, et al. A novel detection method for organophosphorus insecticide fenamiphos: molecularly imprinted electrochemical sensor based on core-shell Co_3O_4@MOF-74 nanocomposite. J Colloid Interface Sci 2021;592:174–85. https://doi.org/10.1016/j.jcis.2021.02.066.
[40] Miraki M, Karimi-Maleh H, Taher MA, Cheraghi S, Karimi F, Agarwal S, et al. Voltammetric amplified platform based on ionic liquid/NiO nanocomposite for determination of benserazide and levodopa. J Mol Liq 2019;278:672–6. https://doi.org/10.1016/j.molliq.2019.01.081.
[41] Karimi-Maleh H, Sheikhshoaie M, Sheikhshoaie I, Ranjbar M, Alizadeh J, Maxakato NW, et al. A novel electrochemical epinine sensor using amplified CuO nanoparticles and a: N -hexyl-3-methylimidazolium hexafluorophosphate electrode. New J Chem 2019;43:2362–7. https://doi.org/10.1039/c8nj05581e.
[42] Karaman O, Özcan N, Karaman C, Yola BB, Atar N, Yola ML. Electrochemical cardiac troponin I immunosensor based on nitrogen and boron-doped graphene quantum dots electrode platform and Ce-doped SnO_2/SnS_2 signal amplification. Mater Today Chem 2022;23. https://doi.org/10.1016/j.mtchem.2021.100666.
[43] Boyacıoğlu H, Yola BB, Karaman C, Karaman O, Atar N, Yola ML. A novel electrochemical kidney injury molecule-1 (KIM-1) immunosensor based covalent organic frameworks-gold nanoparticles composite and porous $NiCo_2S_4$@CeO_2 microspheres: the monitoring of acute kidney injury. Appl Surf Sci 2022;578. https://doi.org/10.1016/j.apsusc.2021.152093.
[44] Karaman C, Karaman O, Atar N, Yola ML. A molecularly imprinted electrochemical biosensor based on hierarchical $Ti_2Nb_{10}O_{29}$ (TNO) for glucose detection. Microchim Acta 2022;189. https://doi.org/10.1007/s00604-021-05128-x.
[45] Karaman C, Karaman O, Yola BB, Ülker İ, Atar N, Yola ML. A novel electrochemical aflatoxin B1 immunosensor based on gold nanoparticle-decorated porous graphene nanoribbon and Ag nanocube-incorporated MoS_2 nanosheets. New J Chem 2021; 45:11222–33. https://doi.org/10.1039/d1nj02293h.
[46] Karaman C, Yola BB, Karaman O, Atar N, Polat İ, Yola ML. Sensitive sandwich-type electrochemical SARS-CoV-2 nucleocapsid protein immunosensor. Microchim Acta 2021:188. https://doi.org/10.1007/s00604-021-05092-6.
[47] Zhang Y, Wang Z, uz Zaman F, Zhao Z, Sun X, Zhang J, et al. Hollow mesoporous hetero-ZnO/$ZnMnO_3$ microspheres: template-free formation process and enhanced lithium storage capability towards Li-ion batteries as a competitive anode. J Mater Chem A 2019;7:3264–77. https://doi.org/10.1039/c8ta10911g.
[48] Chamberland BL, Sleight AW, Weiher JF. Preparation and characterization of $MgMnO_3$ and $ZnMnO_3$. J Solid State Chem 1970;1:512–4. https://doi.org/10.1016/0022-4596(70)90134-9.
[49] Saraf LV, Nachimuthu P, Engelhard MH, Baer DR. Stabilization of $ZnMnO_3$ phase from sol-gel synthesized nitrate precursors. J Sol-Gel Sci Technol 2010;53:141–7. https://doi.org/10.1007/s10971-009-2067-2.
[50] Su X, Huang J, Yan B, Hong Z, Li S, Pang B, et al. Hierarchical porous $ZnMnO_3$ yolk-shell microspheres with superior lithium storage properties enabled by a unique one-step conversion mechanism. RSC Adv 2018;8:31388–95. https://doi.org/10.1039/c8ra05871g.
[51] Kajbafvala A, Shayegh MR, Mazloumi M, Zanganeh S, Lak A, Mohajerani MS, et al. Nanostructure sword-like ZnO wires: rapid synthesis and characterization through a microwave-assisted route. J Alloys Compd 2009;469:293–7. https://doi.org/10.1016/j.jallcom.2008.01.093.
[52] Faraz M, Ansari MZ, Khare N. Synthesis of nanostructure manganese doped zinc oxide/polystyrene thin films with excellent stability, transparency and super-hydrophobicity. Mater Chem Phys 2018;211:137–43. https://doi.org/10.1016/j.matchemphys.2018.02.011.
[53] Senthilkumar N, Venkatachalam V, Kandiban M, Vigneshwaran P, Jayavel R, Vetha Potheher I. Studies on electrochemical properties of hetarolite ($ZnMn_2O_4$) nanostructure for supercapacitor application. Phys E Low-Dimensional Syst Nanostructures 2019;106:121–6. https://doi.org/10.1016/j.physe.2018.10.027.
[54] Shetti NP, Malode SJ, Ilager D, Raghava Reddy K, Shukla SS, Aminabhavi TM. A novel electrochemical sensor for detection of molinate using ZnO nanoparticles loaded carbon electrode. Electroanalysis 2019;31:1040–9. https://doi.org/10.1002/elan.201800775.
[55] Mahmoudian MR, Alias Y, Basirun WJ, Woi PM, Sookhakian M. Facile preparation of MnO_2 nanotubes/reduced graphene oxide nanocomposite for electrochemical sensing of hydrogen peroxide. Sensors Actuators, B Chem 2014;201:526–34. https://doi.org/10.1016/j.snb.2014.05.030.
[56] Mielech-Łukasiewicz K, Staśkowska EB. Sensitive and rapid voltammetric determination of phenothiazine and azaphenothiazine derivatives in pharmaceuticals using a boron-doped diamond electrode. Anal Sci 2015;31:961–9. https://doi.org/10.2116/analsci.31.961.
[57] Mielech-Łukasiewicz K, Puzanowska-Tarasiewicz H, Panuszko A. Electrochemical oxidation of phenothiazine derivatives at glassy carbon electrodes and their differential pulse and square-wave voltammetric determination in pharmaceuticals. Anal Lett 2008;41:789–805. https://doi.org/10.1080/00032710801935038.
[58] Kalanur SS, Jaldappagari S, Balakrishnan S. Enhanced electrochemical response of carbamazepine at a nano-structured sensing film of fullerene-C60 and its analytical applications. Electrochim Acta 2011;56:5295–301. https://doi.org/10.1016/j.electacta.2010.08.071.
[59] Maier Sa. Fundamentals and applications plasmonics : fundamentals and applications, vol. 677; 2004.
[60] Bouchta D, Izaoumen N, Zejli H, El Kaoutit M, Temsamani KR. A novel electrochemical synthesis of poly-3-methylthiophene-γ- cyclodextrin film:

application for the analysis of chlorpromazine and some neurotransmitters. Biosens Bioelectron 2005;20:2228–35. https://doi.org/10.1016/j.bios.2004.12.004.

[61] Tajik S, Garkani-Nejad F, Beitollahi H. Synthesis of La^{3+}/Co_3O_4 nanoflowers for sensitive detection of chlorpromazine. Russ J Electrochem 2019;55:314–21. https://doi.org/10.1134/S1023193519030108.

[62] Ahmadzadeh S, Karimi F, Atar N, Sartori ER, Faghih-Mirzaei E, Afsharmanesh E. Synthesis of CdO nanoparticles using direct chemical precipitation method: fabrication of novel voltammetric sensor for square wave voltammetry determination of chlorpromazine in pharmaceutical samples. Inorg Nano-Metal Chem 2017;47:347–53. https://doi.org/10.1080/15533174.2016.1186049.